This article has been accepted for publication in a future issue of this journal, but has not been fully edited. Content may change prior to final publication. Citation information: DOI 10.1109/TAP.2019.2949135, IEEE Transactions on Antennas and Propagation

Characterization of Propagation Phenomena Relevant for 300 GHz Wireless Data Center Links

Chia-Lin Cheng, *Student Member, IEEE* and Alenka Zajić, *Senior Member, IEEE*

***Abstract*— This paper presents details about an extensive channel measurement campaign and subsequent statistical channel models for the characterization of 300 GHz channels for wireless rack-to-rack (R2R) and blade-to-blade (B2B) communications in a data center-like environment. Measurements were conducted in various scenarios such as R2R line-of-sight (LoS), R2R obstructed-LoS (OLoS), R2R reflected-non-LoS (RNLoS), R2R obstructed-RNLoS (ORNLoS), B2B RNLoS, B2B ORNLoS, and B2B LoS scenarios. In the aforementioned scenarios, we explored the impact of transmitter ($\mathrm{T_x}$)/receiver ($\mathrm{R_x}$) misalignment and obstructions such as cables, metal cabinets, and mesh structures on THz propagation, as well as possibility of using existing metal objects as reflectors that guide waves for NLoS type of links that are prevalent in data centers. For the R2R LoS scenario, an optical lens was used to extend the $\mathrm{T_x}$-$\mathrm{R_x}$ separation distance. This led to a waveguide effect in the channels measured thereby resulting into a path loss exponent (PLE) of 1.48 with a shadowing gain of 0.7 dB. When obstructions of cables are present, ORNLoS link performs better than OLoS link with 2.5 dB lower shadowing gain and weaker multipath. Reflector in the RNLoS link has reflection coefficients very close to 1 for all incident angles. For the B2B scenario, a dual-reflector THz transceiver rack system is proposed to enable wireless links across vertically stacked servers and allow easy maintenance and repair of servers. The measured path loss closely follows the Friis values in the LoS link and in the RNLoS link with hollow vertical ground plane. When obstructions of cables are present, the ORNLoS link experiences 5–10 dB higher path loss and on average 0.25 GHz lower coherence bandwidth than the RNLoS link. Measured statistical channel properties show that the shadowing gain caused by cable clusters follows the log-normal distribution.**

***Index Terms*— THz propagation, wireless propagation in data centers, channel sounding, channel characterization.**

I. INTRODUCTION

Data centers have become a critical component of cloud computing and storage [1], [2]. A fundamental need inside the data centers is reliable and high-speed connectivity between racks and blades [3]. Both metal wires and optical waveguides have been traditionally used in data centers, but they are increasing in assembly cost, maintenance cost, operating cost, service time, and decreasing with regards to cooling efficiency, etc. [1]–[11]. According to [12], cabling cost may take up to 3–8% of the overall infrastructure budget. Cable bundles between server racks and blades can lead to airflow blockages which may cause increased power consumption for cooling or failure of components [13], [14].

One possible solution for data center rack-to-rack (R2R) and blade-to-blade (B2B) links is to use wireless communications. This solution will not only alleviate cable management, serviceability, and packaging constraints, but also reduce latency by providing direct communication [1]–[3], [5]–[11], [15], [16], e.g., from one rack to the rack in the next aisle, as opposed to the common approach of routing cables above racks or down to the floor where they are connected to a router/switch. A key challenge for wireless communication in data centers is that the required data rates in existing systems are already in the hundreds of gigabits per second [17]. Terahertz (THz) wireless communication has several key advantages that can be combined to achieve the required data rates and to facilitate wireless data centers: sufficient available bandwidth [10], [11]—an IEEE 802.15.3d [18] standard for THz communications proposes a data rate up to 100 Gbit/s at 252–325 GHz using eight different bandwidths between 2.16 GHz and 69.12 GHz. Smaller antennas and antenna spacing at THz frequencies enables miniaturization of phased arrays for beamsteering to provide more multiple-input multiple-output (MIMO) channels within the same array aperture to reach Tbit/s data rates. Directionality of propagation at THz frequencies results in reduced interference and increased isolation [19], [20]. Furthermore, data centers provide controllable environmental conditions such as a low moisture atmosphere and limited nodes mobility, which can be favorable for THz wave propagation. The frequency-dependent path loss at THz corresponding to various frequencies and relative humidity levels is presented in [21], [22]. Highly directional antennas can be used to overcome the molecular absorption losses at the THz bands [23]. In addition, optimal carrier frequency selection strategies can reduce path loss and improve throughput [10], e.g., there are several transmission windows around 300 GHz with low atmospheric losses.

To develop THz communication systems, THz propagation needs to be characterized in a data center environment. Since data exchange demands high reliability at data centers, the effects of blockage of cables, humans, and small-scale mobility (e.g. rack vibrations) on THz propagation need to be studied. The blockage caused by cables has been discussed in this paper. Human blockage can cause additional attenuation around 35 dB at 300 GHz [24]. While the effect of rack vibrations depends on antenna beamwidth [25] because rack vibrations may cause $\mathrm{T_x}$-$\mathrm{R_x}$ misalignment up to 0.25 mm [26], however, we have verified that given a THz antenna with a beamwidth at around 10 degrees, a 0.25 mm $\mathrm{T_x}$-$\mathrm{R_x}$ misalignment does not cause any observable time-domain or frequency-domain differences at d = 20–210 cm and thus the effect of rack vibrations is not discussed in this paper. Scattering effect is another important propagation property that

This work has been supported, in part, by NSF grant 1651273. The views and findings in this paper are those of the authors and do not necessarily reflect the views of NSF.

needs to be considered for THz communications as wavelength approximates the surface roughness of the reflecting medium [27]. [28] provides detailed modeling of the diffuse scattering loss and shows that THz wireless links can be established via scattered paths. In our measurements, the R2R RNLoS link experiences scattering of the metal reflector. While the concept of THz wireless data centers has been mentioned in [10], [11], [22], [29] and stochastic channel models for THz wireless data centers have been reported in [11], no channel measurements for THz R2R or B2B communications in data centers have been reported.

This paper presents characterization of 300 GHz channels for wireless R2R and B2B communications in a data center-like environment. We envision that future THz wireless data centers will leverage the integration of B2B and R2R links such that B2B links will provide short-range communication between servers within the same rack, while R2R links with optical lenses enable long-range communication across multiple racks. We have performed measurements in seven different wireless data center scenarios: 1) R2R line-of-sight (LoS); 2) R2R obstructed-LoS (OLoS) with obstructions of cables, metal cabinets, and mesh structures; 3) R2R reflected-non-LoS (RNLoS) link, where a metal reflector is used to guide signals in desired direction; 4) R2R obstructed-RNLoS (ORNLoS) with obstruction of cables placed between the transmitter (T_x)/receiver (R_x) and the reflector; 5) B2B RNLoS, where two metal reflectors are used to direct waves vertically across servers; 6) B2B ORNLoS, where the B2B RNLoS link is obstructed by cables; 7) B2B LoS, where the T_x and R_x are horizontally placed on a rack server. We consider these seven scenarios to evaluate the impact of T_x/R_x misalignment and obstructions such as cables on THz propagation, as well as possibility of using existing metal objects as reflectors that guide signals in NLoS type of links that are prevalent in data centers.

The remainder of this paper is organized as follows. Section II introduces the THz equipment and the PTFE lens configuration. Section III describes seven measurement scenarios. Section IV introduces the analysis methodology. Sections V and VI present measurement and analysis results for R2R and B2B scenarios, respectively. Finally, Section VII provides some concluding remarks.

II. MEASUREMENT SETUP

The measurement setup consists of a Keysight N5224A PNA vector network analyzer (VNA) for recording the frequency-domain channel sounding measurement, a Virginia Diodes, Inc. (VDI) Tx210 transmitter and a VDI Rx148 receiver [30]. The T_x output power is around -15 dBm. The antenna used in the measurement is a vertically polarized pyramidal horn with gain that varies from 22 to 23 dBi from 300 GHz to 312 GHz. The theoretical half-power beamwidth (HPBW) is about 10° in azimuth and elevation. Detailed measurement parameters and instrument description can be found in Table I and [17]. Two plano-convex Polytetrafluoroethylene (PTFE/Teflon) lenses [31] with a focal length of 7.5 cm and a diameter of 5 cm are used in the R2R scenario to collimate the THz beam and provide extra gain. The relative position of lenses and T_x/R_x are shown in Fig. 1. Note that when changing the T_x-R_x distance, the distance between horns and lenses is fixed at 6 cm. Only the distance between two lenses (d') varies.

TABLE I
MEASUREMENT PARAMETERS

Parameter	Symbol	Value
Measurement points	N	801
Intermediate frequency bandwidth	Δf_{IF}	20 kHz
Average noise floor	P_N	-90 dBm
Input signal power	P_{in}	0 dBm
Start frequency	f_{start}	10 MHz
Stop frequency	f_{stop}	12 GHz
Bandwidth	B	11.99 GHz
Time domain resolution	Δt	0.083 ns
Maximum excess delay	τ_m	20 ns

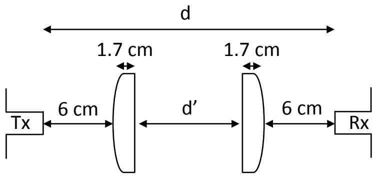

Fig. 1. Plano-convex PTFE lenses configuration for the R2R scenario.

III. MEASUREMENT SCENARIOS

In this measurement campaign, seven wireless data center scenarios have been considered. We envision that future THz wireless data centers will leverage the integration of blade-to-blade (B2B) and rack-to-rack (R2R) links such that B2B links provide short-range communication between servers within the same rack, while R2R links enable long-range communication across multiple racks, and that future THz wireless data center will be equipped with optical lenses and THz transceivers that are miniaturized and integrated into the server chassis. THz beam alignment and beam steering techniques with the use of lenses have been introduced in [32]. The measurement designs and results provided in this paper are the starting point and proof-of-concept for realistic performance evaluations and designs and prototyping of THz communications systems in wireless data center environments. Note that "blade" represents a server mounted on a rack, and the B2B link represents communication link among different servers placed in vertical and horizontal positions on one rack.

A. R2R LoS Link

In the R2R scenario [5], transceivers are mounted on top of the server racks to enable wireless links between racks. Our measurement setup for R2R LoS link is presented in Fig. 2 (a). We place THz T_x/R_x and lenses on top of two separate metal cabinets, where the metal cabinets act as server racks in a data center. The R2R LoS measurements were recorded as the T_x horn-to-R_x horn distance was varied from 40 cm to 210 cm with 5 cm increments, where the maximum distance is limited by the length of the synchronization cable used between the

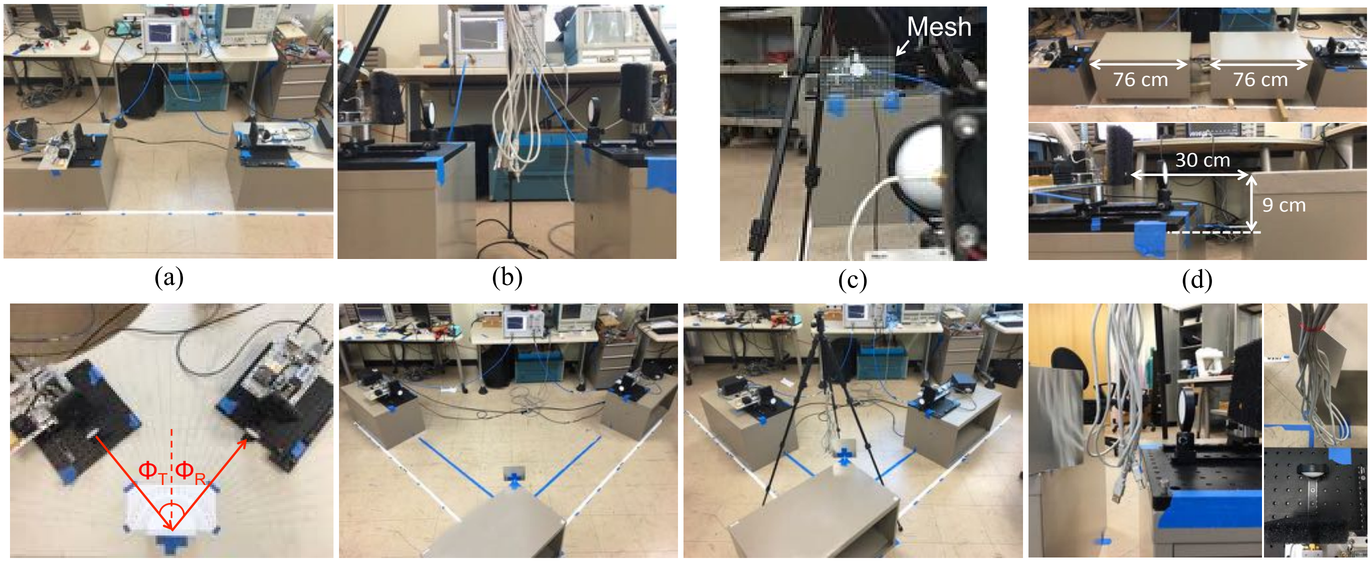

(a) (b) (c) (d)

(e) (f) (g) (h)

Fig. 2. Measurement scenarios of the R2R link: (a) LoS; OLoS with (b) cables, (c) mesh, and (d) metal cabinets serving as obstructions; (e) RNLoS reflection coefficient measurement; (f) RNLoS; (g)/(h) ORNLoS with cables serving as an obstruction.

$\mathrm{T_x}$ and $\mathrm{R_x}$. We use the R2R LoS scenario both as a potential data center link as well as validation of our measurement setup in the R2R obstructed-LoS scenario.

B. R2R OLoS Link

Here we consider a scenario where the wireless channel is obstructed by cables, server racks and their mesh structures, which are common objects in data centers. According to [5], [13], long cables in data centers require overhead cable trays, where cables may be exposed to the R2R link between the overhead cable trays and the racks. The measurement setup for R2R OLoS link with cables as obstruction is presented in Fig. 2 (b). Based on the same setup in Section III-A, we obstruct the LoS channel with a cluster of cables, which are hung in the air from a tripod. By using a tripod to hold cables, we can make sure cables are fixed at the same position (midpoint between $\mathrm{T_x}/\mathrm{R_x}$) while $\mathrm{T_x}/\mathrm{R_x}$ were being moved. The R2R OLoS measurements with cables as obstruction have been recorded at $\mathrm{d} = 40$–210 cm with 10 cm increments. Furthermore, in a data center for an R2R scenario with a maximum distance of 210 cm, there will be multiple server racks between the $\mathrm{T_x}$ and $\mathrm{R_x}$. Multiple metal cabinets and their mesh structures might have an influence on the channel. We have investigated R2R links with metal cabinets and mesh structures placed between the $\mathrm{T_x}$ and $\mathrm{R_x}$ that partially block the channel. The measurement setups for R2R OLoS link with mesh structures and metal cabinets as obstructions are presented in Figs. 2 (c) and (d), respectively. Measurements have been recorded at $\mathrm{d} = 210$ cm.

C. R2R RNLoS Link

R2R RNLoS links are presented to improve the transmission range and allow transceivers to bypass obstacles to communicate directly without multi-hop relays [5]. Most RNLoS links in mm-wave wireless data centers [2], [5]–[7], [11] use the entire ceiling in a server room as reflectors, which takes huge space and increases cost. Our measurement setup in Fig. 2 (f) demonstrates that to enable a R2R RNLoS link in a THz wireless data center, a palm-sized compact reflector would be sufficient due to the extremely focused THz beam. If more links are required, we may increase the size of the reflector or cover the ceiling/wall with reflecting material and use them as reflectors [2], [5]–[7], [11]. Note that the geometry of the reflector needs to accommodate the size of the lens. We have designed an aluminum square-shape reflector with a side length of 15 cm, which is roughly twice the lens diameter. The R2R RNLoS measurements have been recorded at $\mathrm{T_x}$ horn-to-reflector-to-$\mathrm{R_x}$ horn distance $= 40$–210 cm with 5 cm increments with equal $\mathrm{T_x}/\mathrm{R_x}$-to-reflector distances and equal transmitting and receiving angles (ϕ_T/ϕ_R) at 45°. We use the R2R RNLoS scenario as validation of our measurement setup for the R2R RNLoS that we later used for the obstructed-RNLoS scenario. Furthermore, we also characterized the reflection coefficient and the angular misalignment tolerance range of the aluminum reflector used in the R2R RNLoS link with the measurement setup in Fig. 2 (e). In the reflection coefficient measurement, to ensure specular reflection, the angle of incidence (ϕ_T) is set equal to the angle of reflection (ϕ_R) in the range from 20° to 85° in 5° increments with $\mathrm{T_x}$ horn-to-reflector-to-$\mathrm{R_x}$ horn distance fixed at 90 cm. This setup is chosen to test the stability of the reflector's reflection coefficient in various $\mathrm{T_x}/\mathrm{R_x}$ angular setups since in reality the R2R RNLoS link may not be able to position the reflector at exact $\phi_T = \phi_R = 45°$, e.g., obstructions or location of the racks may vary. In the angular misalignment measurement, ϕ_T is fixed at 45° while ϕ_R varied from 5° to 85° in 5° increments with $\mathrm{T_x}$ horn-to-reflector-to-$\mathrm{R_x}$ horn distance fixed at 90 cm. This setup is chosen to test the angular misalignment tolerance range.

D. R2R ORNLoS Link

Our measurement setup for the R2R ORNLoS link with cables as obstruction is presented in Figs. 2 (g) and (h). Similar to the setup in Section III-C, here we place a tripod with obstructing cables between the T_x and the reflector. The R2R ORNLoS measurements have been recorded at d = 40–210 cm with 10 cm increments.

E. B2B RNLoS Link

In the B2B RNLoS scenario, rack-mounted reflectors are used to enable wireless links across vertically stacked servers. Optical lenses are not applied due to shorter communication range and limited space in a B2B environment. Fig. 3 (a) and Figs. 4 (a)–(d) present schematics and measurement setup of the B2B RNLoS link. Note that the rack in Fig. 4 is a mock-up of a real server rack. T_x is placed at the lower blade (blade 2) and R_x is placed at the upper blade (blade 1), both of which are facing toward the vertical metal panel of the cabinet. To enable a link between T_x and R_x, we position two rack-mounted reflectors in a similar manner as in a periscope, i.e., two reflectors are positioned at 45° to the direction where T_x and R_x are pointed to, such that the transmitted signal can reach the R_x via a vertical channel between two vertically aligned reflectors. Using metal reflectors for communication between two blades can be extended to multiple blades by having longer metal reflectors. Many of the datacenter racks come with metal enclosure that can be leveraged as a reflector. Data exchange at each server node is typically point-to-point communication, where a switch will be used to connect multiple servers onto the network. Interference may need to be handled for the coexistence of multiple B2B links. Fortunately, due to the narrow beamwidth at THz frequencies, interference can be better managed compared to lower frequencies. One advantage of using rack-mounted reflectors as compared to waveguides is that it allows easy maintenance and repair of blades. In addition, we want to test the possibility of using reflectors for NLoS type of link inside a server rack since there may be obstacles inside server compartments blocking the propagation path, which require redirecting the THz beam. Reflectors will provide more flexibility for realizing NLoS type of links inside a server rack. In Fig. 3 (a), d1 = d3 are the T_x/R_x-to-reflector distance, d2 = 15 cm is the distance between the T_x- and R_x-reflectors (roughly twice/four times of the height of the 2U/1U rackmount servers [33]), d4 = 4 cm is the gap between rack's vertical ground plane and the edge of the reflector, d5 = 2.2 cm is the distance between the horizontal ground plane and the horn center. We have found that reflection can be generated from both vertical and horizontal ground planes inside the rack (paths 1, 2, and 3 in Figs. 3 (b) and (c)) and can lead to significant path loss variation as distance increases. To better understand the reflection in a B2B environment, we conducted our experiments with three vertical ground plane designs in a server compartment: 1) solid metal (Fig. 5 (a)), 2) hollow (Fig. 5 (b)), and 3) mesh (Fig. 5 (c)) structures. Since we want to focus on analyzing reflection from the vertical ground plane, we limit the total distance (d = d1 + d2 + d3) to within 49 cm such that the reflection interference from blade 2's horizontal ground plane (path 3 in Fig. 3 (c)) can be minimized. The server rack we use has a dimension of 130 cm x 75 cm x 45 cm. The opening window of the vertical ground plane (Fig. 5) has a size of 12 cm x 10 cm. The T_x/R_x reflectors are made of aluminum and have dimensions of 15 cm x 5 cm. Note that the size of reflectors should accommodate the height and the beamwidth of the T_x/R_x antennas, and that the alignment of T_x/R_x reflectors is critical since the received signal is extremely sensitive to the positioning of the reflectors. We briefly discuss the consequences of misaligned reflectors in the following paragraphs. The B2B RNLoS measurements have been recorded as the total horn-to-horn distance (d = d1 + d2 + d3) varied from 20 cm to 49 cm with 1 cm increments (both d1 and d3 change and d1 = d3).

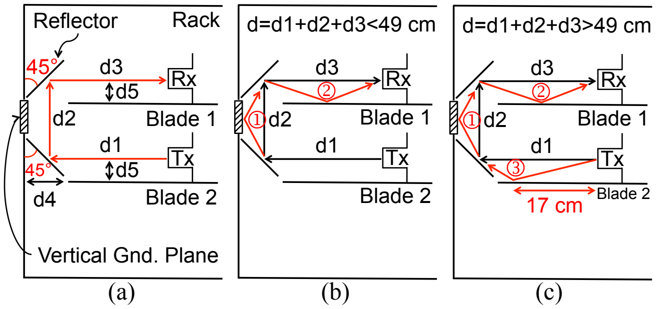

(a) (b) (c)

Fig. 3. (a) Schematics of B2B RNLoS measurement setup. Analysis of reflection interference in B2B environment at (b) d < 49 cm and (c) d > 49 cm.

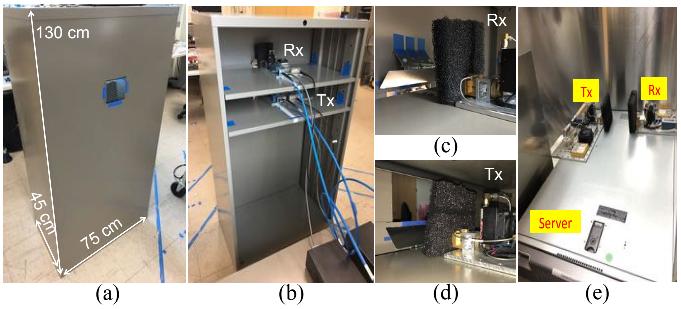

(a) (b) (c) (d) (e)

Fig. 4. Measurement setup of the vertical B2B link: (a) back and (b) front sides of the rack, (c) R_x and R_x-reflector at the upper blade, (d) T_x and T_x-reflector at the lower blade; (e) measurement setup of the B2B LoS link.

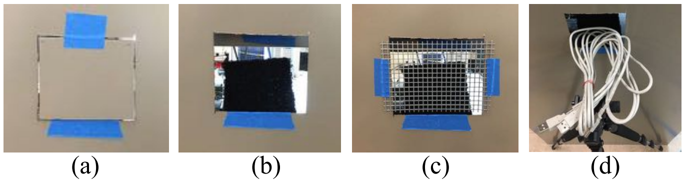
(a) (b) (c) (d)

Fig. 5. Vertical ground plane designs in B2B server compartments: (a) solid metal, (b) hollow structure, and 3) mesh structure; (d) hollow structure with cables as obstruction.

F. B2B ORNLoS Link

Our measurement setup for the B2B ORNLoS link is presented in Fig. 5 (d). Similar to the setup in Section III-E, here we place the obstructing cables supported by a tripod through the opening window of the vertical ground plane between the T_x- and R_x-reflectors. The B2B ORNLoS measurements have been recorded at d = 20–49 cm with 1 cm increments.

G. B2B LoS Link

Our measurement setup for the B2B LoS link is presented in Fig. 4 (e), where the T_x and R_x are placed on a rack server and aligned horizontally as common blade servers are placed on a rack. Aluminum plates are placed around the rack server to mimic a rack compartment environment. The B2B LoS measurements have been recorded at d = 12, 14, 16, and 18 cm. $\mathrm{T_x}$-$\mathrm{R_x}$ distances are selected such that they are greater than the thickness of one blade server (4.4 cm for one blade according to [33]) or multiple blade servers.

IV. ANALYSIS METHODOLOGY

A. Path Loss and Multipath Characterization

In this paper, the mean of measured path loss, $\overline{PL}$, is obtained by averaging a swept continuous wave over time and frequency, i.e.,

$$\overline{PL(d)} = \frac{1}{MN}\sum_{i=1}^{N}\sum_{j=1}^{M}|H(f_i,t_j,d)|^2, \tag{1}$$

where $H(f_i,t_j,d)$ is the measured complex frequency response data (transfer function), M is the number of frequency-response snapshots over time, N is the number of observed frequencies, and d is the $\mathrm{T_x}$-$\mathrm{R_x}$ horn-to-horn separation distance. We model the mean path loss by the single-frequency floating-intercept (FI, alpha-beta, or the 3rd Generation Partnership Project 3GPP) model due to better susceptibility to measurement errors [34]. The FI path loss model is given as follows [35, pp. 16–21]:

$$PL^{FI}(d) = \alpha + 10\beta\log_{10}\left(\frac{d}{d_0}\right) + X_\sigma^{\mathrm{FI}}, d \geq d_0, \tag{2}$$

where $PL^{FI}(d)$ is the path loss in dB as a function of d, α is a floating intercept in dB that represents the free-space path loss at the reference distance d_0 = 20 cm. According to [36], d_0 should always be in the far-field of the antenna so that the near-field effects do not alter the reference path loss. The far-field boundary in our work was estimated as 4.23 cm at 300 GHz according to the Fraunhofer distance given that the largest physical dimension of the horn aperture is 4.6 mm. We set d_0 as 20 cm since it falls within the far-field range and it is also the first distance measured in our work. β is the path loss exponent (PLE) that characterizes the dependence of path loss on d, and X_σ^{FI} is the large-scale shadowing gain that can be modeled as a zero-mean Gaussian distributed random variable with standard deviation σ in dB. To estimate the path loss model parameters α, β, and σ, the least-squares linear fitting is performed through the measured path loss data sets such that the root mean square (RMS) deviation from the mean path loss is minimized.

The channel impulse response is obtained by taking the inverse discrete Fourier transform (IDFT) of the measured channel frequency response. Root-mean-square (RMS) delay spread is calculated by taking the square root of the second central moment of the normalized squared magnitude of the channel impulse response, i.e.,

$$\tau_{rms} = \sqrt{\sum_{k=1}^{L}(\tau_k - \tau_m)^2|h(t,\tau_k,d)|^2}, \tag{3}$$

where L is the number of multipath components, τ_k is the excess delay of the k^{th} path relative to the first arrival, $|h(t,\tau_k,d)|^2$ is the squared magnitude of the channel impulse normalized by the sum of PDPs over delay bins, and τ_m is the mean excess delay defined as

$$\tau_m = \sum_{k=1}^{L}\tau_k\cdot|h(t,\tau_k,d)|^2. \tag{4}$$

The coherence bandwidth (B_c) with a correlation coefficient of 0.9 is estimated as [36],

$$B_c \approx 1/(2\cdot\pi\cdot\tau_{rms}). \tag{5}$$

B. Reflection Coefficients

The reflection loss of the aluminum reflector in the R2R link is obtained by calculating the difference between the R2R LoS received power at d = 90 cm and the R2R RNLoS received power with $\phi_T = \phi_R = 45°$ and $\mathrm{T_x}$ horn-to-reflector-to-$\mathrm{R_x}$ horn distance at 90 cm. The reflection coefficient is found from the reflection loss,

$$RL = -20\log_{10}|\Gamma|, \tag{6}$$

where Γ is the reflection coefficient and RL is the reflection loss in dB, which is calculated from the link budget equation,

$$RL = P_t - P_r + G_t + G_r - \overline{PL} \quad [dB]. \tag{7}$$

Note that similar characterization of the reflectors in the B2B RNLoS link without $\mathrm{T_x}$/$\mathrm{R_x}$ optical lenses can be found in [37].

V. R2R RESULTS

A. Characterization of R2R LoS and R2R RNLoS Links

In this section, we investigate the relationship between $\mathrm{T_x}$-$\mathrm{R_x}$ distance and the corresponding path loss, PDPs, and B_c in the R2R LoS and R2R RNLoS scenarios as introduced in Figs. 2 (a), (f) and Sections III-A and III-C.

For the path loss measurements, Figs. 6 (a) and (b) present the measured path loss with $\mathrm{T_x}$-$\mathrm{R_x}$ distances varying from 50 cm to 210 cm in R2R LoS and R2R RNLoS scenarios, respectively. We can observe that LoS and RNLoS links have similar path loss values that range between 50–64 dB at distances between 50–210 cm. Friis theoretical path loss at d = 50 cm is also presented in Figs. 6 (a) and (b) to demonstrate that more than 25 dB additional gain can be obtained with the use of optical lenses. Note that due to the very focused beam created by the lenses, the channel characteristics (e.g. multipath, ripples in transfer function) in the R2R scenarios are dominated by the effects of the lenses rather than the surrounding environment. As a result, we will include the lenses as part of the propagation channel rather than part of the measurement system. Periodic ripples in the measured path loss curves are the strongest at shorter distances and gradually attenuate as distance increases. This is because the periodic ripples are caused by multiple reflections between lenses and horns that gradually decay as the distance increases. Note that the periodic path loss ripples with peak-to-peak values up to 4 dB are not caused by the antenna gain diagram since the peak-to-peak antenna gain variations over frequency are only around 0.6 dB.

For the analysis of path loss models, Fig. 7 presents the measured mean path loss and FI path loss models for the R2R

This article has been accepted for publication in a future issue of this journal, but has not been fully edited. Content may change prior to final publication. Citation information: DOI 10.1109/TAP.2019.2949135, IEEE Transactions on Antennas and Propagation

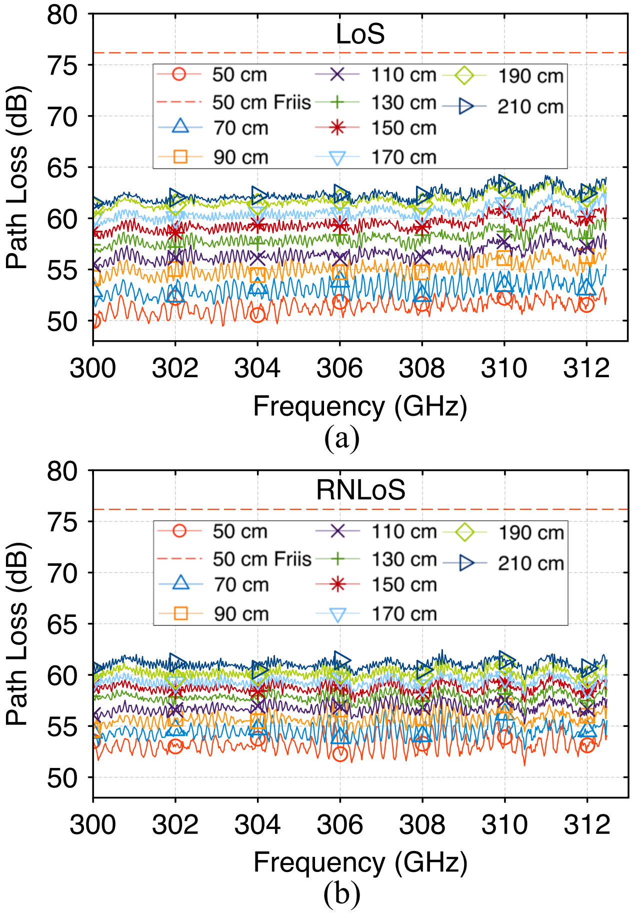

(a)

(b)

Fig. 6. Measured path loss curves in (a) R2R LoS and (b) R2R RNLoS scenarios at d = 50, 70, 90, 110, 130, 150, 170, 190, 210 cm along with Friis theoretical path loss at d = 50 cm.

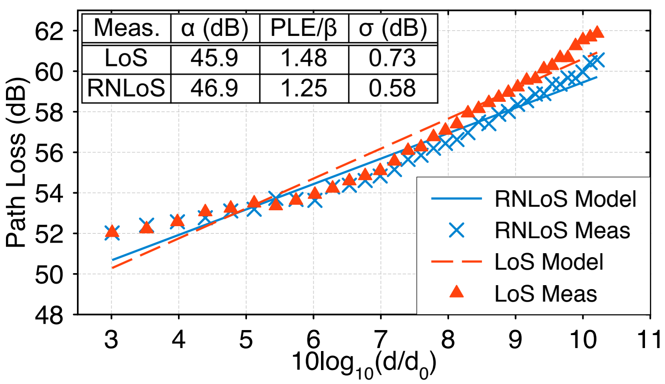

Meas.	α (dB)	PLE/β	σ (dB)
LoS	45.9	1.48	0.73
RNLoS	46.9	1.25	0.58

Fig. 7. Measured mean path loss for the R2R LoS (red triangles) and R2R RNLoS (blue cross signs) scenarios and FI path loss models for the R2R LoS (red dash line) and the R2R RNLoS (blue solid line) scenarios at d = 40–210 cm and d_0 = 20 cm.

LoS and R2R RNLoS scenarios at d = 40–210 cm. Detailed path loss model parameters are summarized in Fig. 7. It can be observed that the R2R RNLoS link has similar path loss values as the R2R LoS link. We can also observe that both the R2R LoS and the R2R RNLoS links act as waveguides with PLEs of 1.48 and 1.25 due to the use of optical lenses. Interestingly, we found that both R2R LoS link (red triangles in Fig. 7) and R2R RNLoS link (blue cross signs in Fig. 7) seem to have two trends of slopes (PLE): one from 3 to 6 dB of x-axis and the other from 6 to 10 dB of x-axis. From 3 to 6 dB of x-axis, both R2R LoS and R2R RNLoS links have similar slopes of around 0.5. From 6 to 10 dB of x-axis, the R2R LoS link has a slope of around 2, whereas the slope is around 1.6 in the R2R RNLoS link. We conclude that two trends of slopes in the R2R LoS and R2R RNLoS links result from the diverging of the beam given the fact that the collimated beam created by the lenses is not perfectly parallel. At distance between 40 cm and 80 cm (from 3 to 6 dB of x-axis), the diverging of the collimated beam is less significant and thus the R2R LoS link and the R2R RNLoS link have similar path loss values and slopes. In contrast, at distance between 80 cm and 210 cm (from 6 to 10 dB of x-axis), the collimated beam diverges to an extent such that the received signal starts to decay at a faster rate for both R2R LoS and R2R RNLoS links. Specifically, for the R2R LoS link, the received signal decays at a rate similar to in a free space with a path loss slope (PLE) of around 2, while for the R2R RNLoS link, the reflector helps to "collect" these diverged waves and transmit them from the $\mathrm{T_x}$ to the $\mathrm{R_x}$ and thus leads to lower path loss values and a path loss slope (PLE) of around 1.6.

Figure 8 shows the measured PDPs for R2R LoS and R2R RNLoS scenarios at d = 50–210 cm. Distinctive multipaths can be categorized into three clusters labeled as 1, 2, and 3 in Figs. 8 (a) and (b). Cluster 1 results from reflections between ($\mathrm{T_x}$ lens and $\mathrm{T_x}$ horn) and ($\mathrm{R_x}$ lens and $\mathrm{R_x}$ horn), where a time delay of 0.8 ns corresponds to four times of lens-horn distance. Note that cluster 1 does not move as distance increases since the lens-horn distance is fixed at 6 cm as shown in Fig. 1. Cluster 2 is a combination of reflections between $\mathrm{T_x}$ lens and $\mathrm{R_x}$ horn and between $\mathrm{R_x}$ lens and $\mathrm{T_x}$ horn. Take the R2R LoS 50 cm PDP curve (red curve in Fig. 8 (a)) for example, cluster 2 has a delay about 3 ns corresponding to an additional delay path of 90 cm that is roughly twice the distance from the $\mathrm{R_x}$ horn to the $\mathrm{T_x}$ lens plus multiple reflected paths within the $\mathrm{R_x}$ lens. Cluster 3 is due to $\mathrm{R_x}$ horn-to-$\mathrm{T_x}$ horn reflection. Take the R2R LoS 50 cm PDP curve (red curve in Fig. 8 (a)) for example, it can be observed that cluster 3 has a delay around 3.7 ns corresponding to an additional delay path of 111 cm that is roughly twice the distance from the $\mathrm{R_x}$ horn to the $\mathrm{T_x}$ horn plus multiple reflected paths within the $\mathrm{R_x}$ lens and the $\mathrm{T_x}$ lens. Since the surrounding area of the $\mathrm{T_x}$ and $\mathrm{R_x}$ horns are covered with absorbers, we can conclude that the horn-related multiple reflections come from the tips and internal surfaces of the horns. In Figs. 8 (a) and (b), it can be observed that as distance gradually increases, clusters 2 and 3 in the R2R LoS link and cluster 3 in the R2R RNLoS link gradually decayed below the noise floor (cluster 3 decayed at a faster rate than cluster 2), while cluster 2 in the R2R RNLoS link still remains observable. As distance increases to 185–210 cm, only cluster 1 in the R2R LoS link remained as shown in Fig. 8 (a). In contrast, both clusters 1 and 2 in the R2R RNLoS link remained observable at distance up to 210 cm as shown in Fig. 8 (b) at around 12–14 ns. The comparison in Figs. 8 (a) and (b) shows that the reflector in R2R RNLoS link preserved reflections between $\mathrm{T_x}$ lens and $\mathrm{R_x}$ lens and sustained cluster 2 in PDPs across distances of 50–210 cm. This difference in PDPs between R2R LoS and R2R RNLoS links has an impact on the B_c values and the maximum data

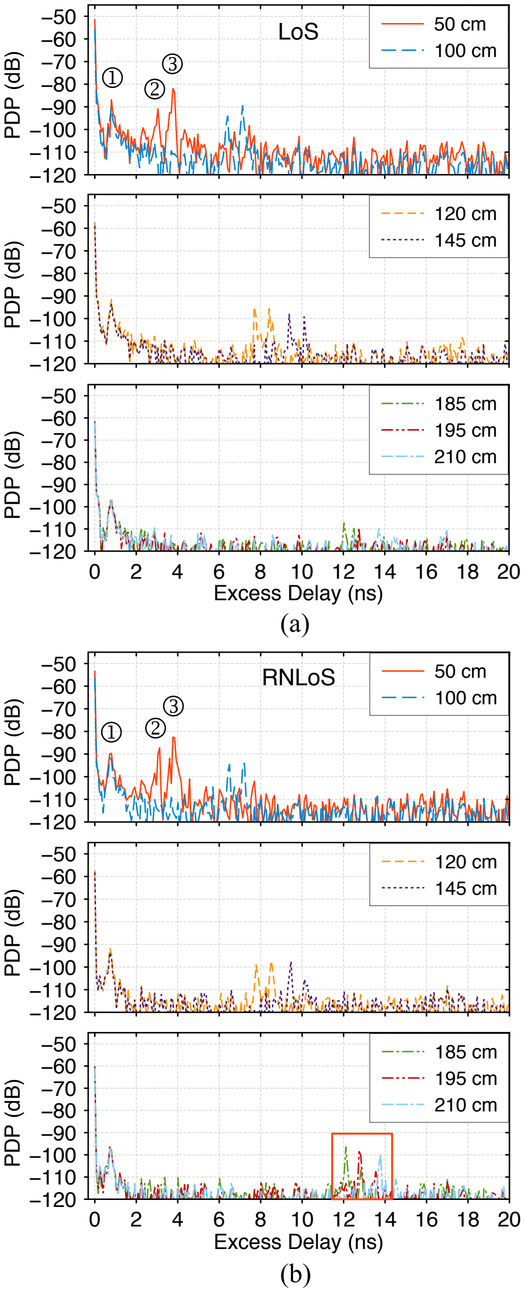

(a)

(b)

Fig. 8. Measured PDPs for (a) R2R LoS and (b) R2R RNLoS scenarios at d = 50, 100, 120, 145, 185, 195, 210 cm.

rate as discussed in the next paragraph. In addition, we can infer that reflections from server rack frames (metal cabinets in our mock-up) are insignificant in the R2R LoS and R2R RNLoS links since the dominant multipath clusters 1, 2, and 3 are from reflections between the lenses.

B_c is a key parameter whose value is relative to the available bandwidth and data rate of the transmitted signal, thereafter determines the need for employing channel protection techniques, e.g., channel equalization, channel coding, or channel diversity to overcome the dispersive effects of multipaths [38]. In this paper, B_c is estimated from τ_{rms} with a correlation coefficient of 0.9 using (5). When calculating τ_{rms} from PDP, we perform noise filtering on PDP to remove unwanted noise by setting a threshold level at 8 dB above the noise floor, where PDP values below this threshold are considered as noise and equaled to zero. Fig. 9 shows the measured B_c for R2R LoS and R2R RNLoS scenarios at d = 40–210 cm. An overall trend of increasing B_c as distance increases is observed in both LoS and RNLoS links, which is counterintuitive because τ_{rms} is expected to increase as distance increases due to wider beamwidth coverage of surrounding objects at further distance, resulting in decreased B_c. This counterintuitive observation results from the highly focused beam created by the lenses used in our measurement. Optical lenses effectively collimate the beam such that the propagating wave stays within the "cylindrical tube" created by the lenses. Because of this confined "tube-like" propagation channel, even though the distance increases, there is no additional multipath involved in the channel except for clusters 1, 2, and 3 shown in Fig. 8. As distance increases, the existing clusters 1, 2, and 3 are attenuated thereby leading to a reduction in τ_{rms} and an increment in B_c. If we look into Fig. 9 more carefully, at distance around 60-180 cm, the RNLoS link has a slightly higher B_c than the LoS link. This is mostly due to reflector's reflection loss (shown in Fig. 16). At d = 60-180 cm, the amplitude of multipath clusters 1, 2, and 3 in the RNLoS link in Fig. 8 (b) is slightly lower than that in the LoS link in Fig. 8 (a) due to reflection loss of the reflector. The attenuated multipath in the RNLoS link leads to a slightly lower τ_{rms} and slightly higher B_c. Similar observation is found in the obstructed R2R links in Fig. 12, where on average B_c in the ORNLoS link is slightly higher than the OLoS link due to suppressed multipath. Now if we compare the B_c in Fig. 9 at distance beyond 180 cm, it is observed that the B_c in the LoS link is higher than the RNLoS link by approximately 1 GHz. The suppressed B_c in the RNLoS link is caused by the scattering effect of the metal reflector. According to [39], metal objects can be viewed as perfect electrical conductors with a slightly rough surface and can cause scattering in the THz frequencies. The reflector in the RNLoS link slightly scatters the beam such that the beam is no longer ideally confined within the "tube-like" propagation channel and is reflected off of the metal rim of the lenses. As a result, multipath cluster 2 in the RNLoS link remains observable even at distances beyond 180 cm (highlighted in Fig. 8 (b)) due to reflections from the lens rim, resulting in higher τ_{rms} and lower B_c. Narrower B_c in the R2R RNLoS link may limit the maximum data rate.

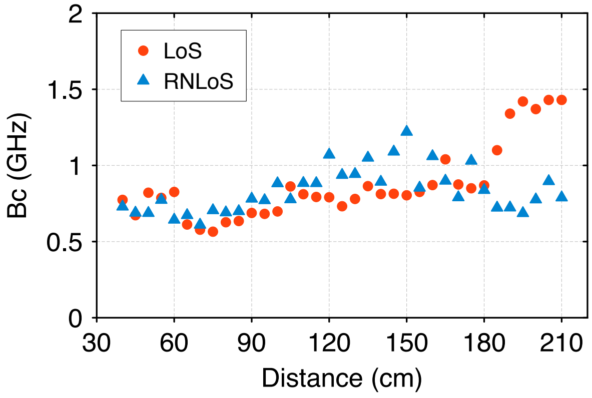

Fig. 9. Measured B_c for R2R LoS and R2R RNLoS scenarios at d = 40–210 cm.

This article has been accepted for publication in a future issue of this journal, but has not been fully edited. Content may change prior to final publication. Citation information: DOI 10.1109/TAP.2019.2949135, IEEE Transactions on Antennas and Propagation

B. Characterization of R2R OLoS and R2R ORNLoS Links

In this section, we study the relationship between T_x-R_x distance and the corresponding path loss, PDPs, and B_c in the R2R OLoS link with cables, mesh structures, and metal cabinets as obstructions and the R2R ORNLoS link with cables as obstruction introduced in Figs. 2 (b), (g), (h), and Sections III-B and III-D.

Figures 10 (a) and (b) compare the Friis path loss and the measured path loss in R2R OLoS and R2R ORNLoS links with cables as obstruction at d = 50, 110, 150, 210 cm. It is observed that the R2R ORNLoS link achieves lower path loss (5 dB lower at distance beyond 1.3 m) and less path loss fluctuations with frequency as compared to the R2R OLoS link. Since the radius of the curvature of the cables are comparable to the wavelength at 300 GHz, the wave experiences a combination of reflection and diffraction as propagating through cables. The reflector in R2R ORNLoS link helps to "collect" these reflected and diffracted waves and transmit them from the T_x to the R_x and thus leads to lower path loss as compared to the R2R OLoS link. Figures 11 (a) and (b) show the measured PDPs for R2R OLoS and R2R ORNLoS links at d = 50, 110, 150, 210 cm. It is observed that the most of the dominant multipath clusters (clusters 2 and 3) in Figs. 8 (a) and (b) are no longer observable in the presence of obstructing cables. Figure 12 shows the measured B_c for R2R OLoS and R2R ORNLoS scenarios at d = 40–210 cm. It is observed that as distance increases from 40 cm to 210 cm, B_c drops from around 1.5–1.8 GHz to around 0.3–0.8 GHz. The R2R ORNLoS link has a wider B_c than the R2R OLoS link, corresponding to a relatively flat frequency domain response in Fig. 10 (b) compared to Fig. 10 (a), due to R2R ORNLoS link's suppressed multipath as shown in Figs. 11 (a) and (b).

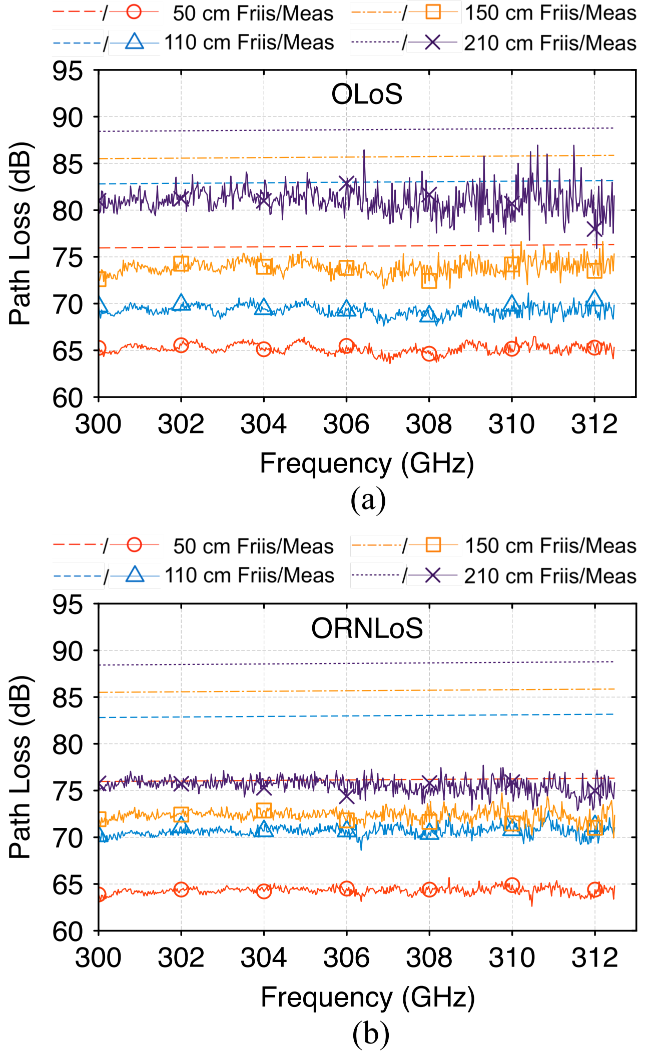

(a)

(b)

Fig. 10. Measured path loss curves in (a) R2R OLoS and (b) R2R ORNLoS scenarios with cables as obstruction at d = 50, 110, 150, 210 cm.

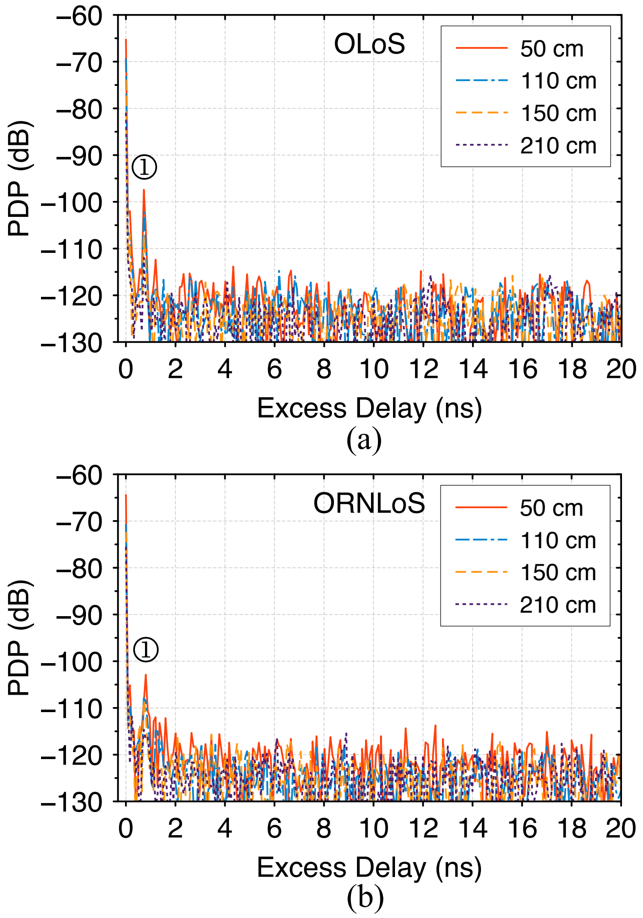

(a)

(b)

Fig. 11. Measured PDPs for (a) R2R OLoS and (b) R2R ORNLoS scenarios with cables as obstruction at d = 50, 110, 150, 210 cm.

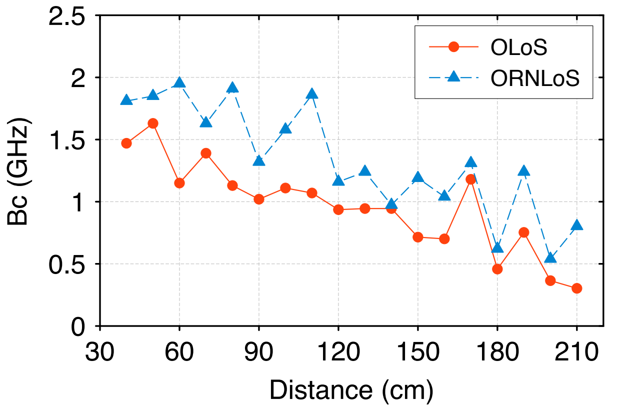

Fig. 12. Measured B_c for R2R OLoS and R2R ORNLoS scenarios with cables as obstruction at d = 40–210 cm.

This article has been accepted for publication in a future issue of this journal, but has not been fully edited. Content may change prior to final publication. Citation information: DOI 10.1109/TAP.2019.2949135, IEEE Transactions on Antennas and Propagation

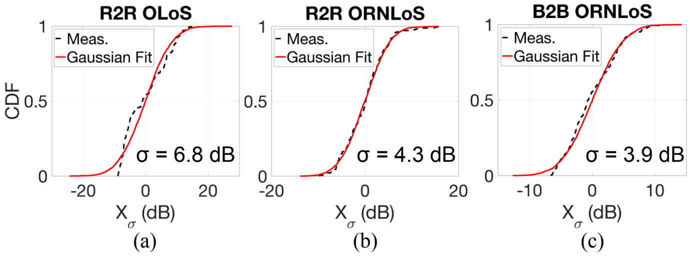

(a) (b) (c)

Fig. 13. CDFs of the shadowing gain (X_σ) for (a) R2R OLoS link at d = 40–210 cm, (b) R2R ORNLoS link at d = 40–210 cm, (c) B2B ORNLoS link at d = 20–49 cm, all measured with three cable thickness sizes and ten cable positions.

We have further investigated the shadowing gain (X_σ) in the R2R OLoS and the R2R ORNLoS links with cables as obstructions by repeating the measurements with three cable thickness sizes and ten cable positions at d = 40–210 cm to have enough ensemble to perform a statistical evaluation. We found that the shadowing gain of both R2R OLoS and the R2R ORNLoS links follow log-normal distribution with its logarithmic equivalent having a zero-mean (in dB) and standard deviations (σ) of 6.8 dB and 4.3 dB, respectively. Cumulative distribution functions (CDFs) of X_σ for both links are presented in Figs. 13 (a) and (b) to confirm the log-normality of the shadowing gain.

Figure 14 presents the measured path loss at d = 210 cm in the R2R LoS link (scenario in Fig. 2 (a); red circles) and in the R2R OLoS links with obstructions of mesh structures (scenario in Fig. 2 (c); green cross signs) and metal cabinets (scenario in Fig. 2 (d); blue triangles). Friis path loss at d = 210 cm is presented alongside as a reference (red dash curve). Additional path loss of around 3 dB and 10 dB were observed due to the obstructions of mesh structures and metal cabinets, respectively. Fig. 15 shows the measured PDPs at d = 210 cm in the R2R LoS link (red curve) and in the R2R OLoS links with obstructions of mesh structures (blue dash curve) and metal cabinets (purple dot curve). Two dominant multipaths have been observed: 1) multipath 1 is located at around 0.8 ns (same cause as cluster 1 in Fig. 8) and is present in all scenarios; 2) multipath 2 is only present in the R2R OLoS link obstructed by metal cabinets and is located at around 2 ns, which corresponds to two times of the distance (30 cm) between the middle cabinets and the $\mathrm{T_x}$/$\mathrm{R_x}$ racks as shown in Fig. 2 (d).

C. *Characterization of Reflection Coefficients of Reflectors*

In this section, we characterize the reflection loss and the reflection coefficient of the aluminum reflector used in the R2R RNLoS link with optical lenses applied to the $\mathrm{T_x}$/$\mathrm{R_x}$. Similar characterization of the reflectors in the B2B RNLoS link without $\mathrm{T_x}$/$\mathrm{R_x}$ optical lenses can be found in [37]. Our measurement setup is introduced in Fig. 2 (e) and Section III-C. Calculation of reflection loss and reflection coefficient is explained in Section IV-B.

Figure 16 presents the measured reflection loss of the aluminum reflector used in the R2R RNLoS link. Averaged reflection loss is calculated as 0.6 dB across the measured frequencies (from 300 GHz to 312 GHz). Fig. 17 (a) and Fig. 18 (red circles) present the measured path loss and the magnitude of reflection coefficient of the aluminum reflector used in the R2R RNLoS link with $\phi_T = \phi_R =$ 20°, 40°, 45°, 50°, 70°. It is observed that the measured path loss values approximate 55 dB, which result in reflection coefficients very close to 1 across all ϕ_T and ϕ_R angles. Fig. 17 (b) and Fig. 18 (blue triangles) present the measured path loss and the magnitude of reflection coefficient of the aluminum reflector used in the R2R RNLoS link with ϕ_T fixed at 45° while ϕ_R varies at 20°, 40°, 45°, 50°, 70°. It is observed that as ϕ_R deviates from ϕ_T by only 5° (from $\phi_R = 45°$ to 40° or 50°), path loss increases more than 20 dB and reflection coefficient decreases from around 1 to less than 0.1 due to very focused beam. We can conclude that the reflector serves as a good reflecting surface for reliable RNLoS links at all angles (ϕ_T = ϕ_R). However, angular misalignment ($\phi_T \neq \phi_R$) requires careful attention in RNLoS links in THz wireless data centers given that the angular misalignment tolerance range is less than 5°.

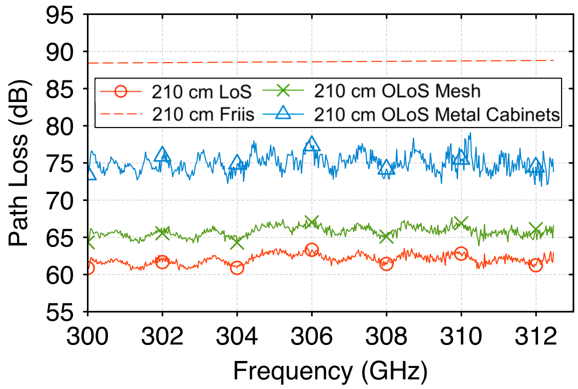

Fig. 14. Measured path loss curves at d = 210 cm in the R2R LoS link (red circles) and in the R2R OLoS links with obstructions of mesh structures (green cross signs) and metal cabinets (blue triangles). Friis path loss at d = 210 cm is presented alongside as a reference (red dash curve).

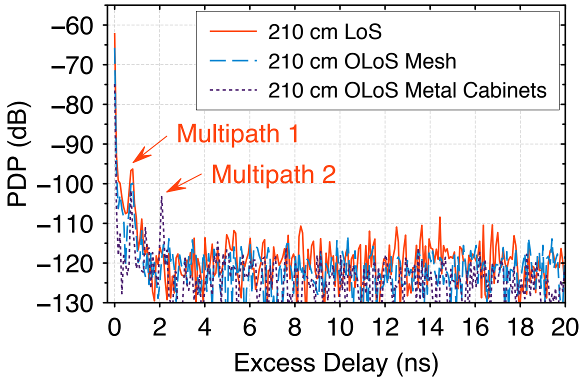

Fig. 15. Measured PDPs at d = 210 cm in the R2R LoS link (red curve) and in the R2R OLoS links with obstructions of mesh structures (blue dash curve) and metal cabinets (purple dot curve).

VI. B2B RESULTS

A. *Characterization of B2B RNLoS and B2B ORNLoS Links*

In this section, we investigate the reflection from different vertical ground plane structures and the relationship between $\mathrm{T_x}$-$\mathrm{R_x}$ distance and the corresponding path loss, PDPs, and B_c in the B2B RNLoS and B2B ORNLoS scenarios as introduced in Figs. 3–5 and Sections III-E and III-F.

Figure 19 presents the Friis theoretical path loss (red line) and the measured mean path loss with different vertical ground

This article has been accepted for publication in a future issue of this journal, but has not been fully edited. Content may change prior to final publication. Citation information: DOI 10.1109/TAP.2019.2949135, IEEE Transactions on Antennas and Propagation

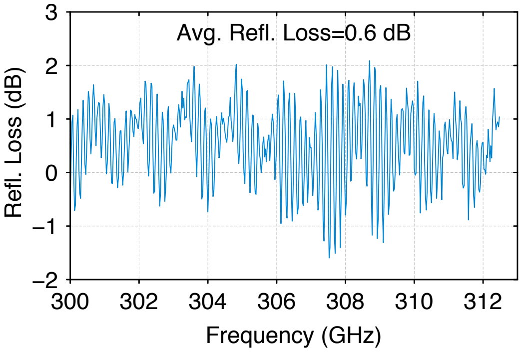

Fig. 16. Measured reflection loss of the aluminum reflector used in the R2R RNLoS link. The averaged reflection loss is calculated as 0.6 dB.

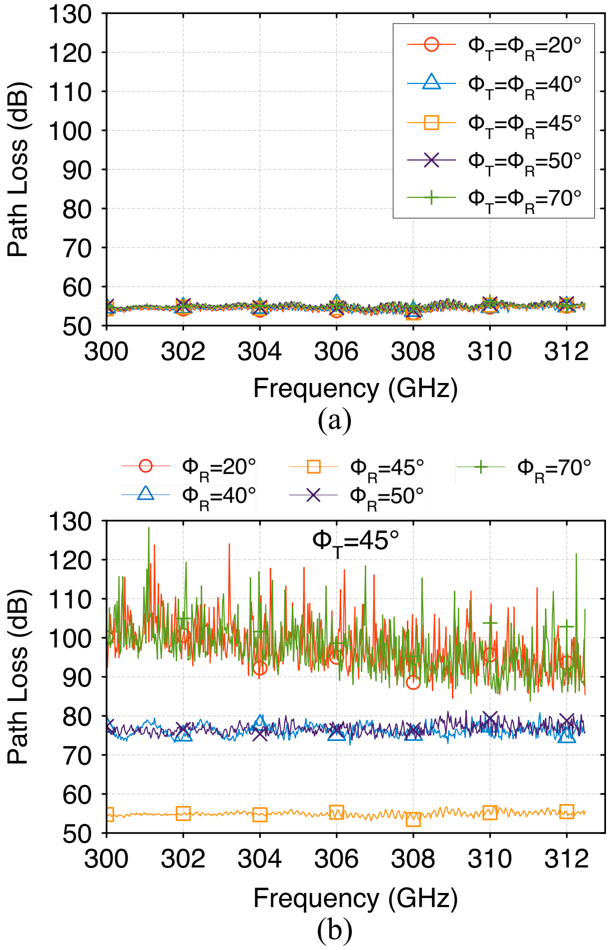

(a)

(b)

Fig. 17. Measured path loss in the R2R RNLoS link at d = 90 cm with (a) $\phi_T = \phi_R = 20°, 40°, 45°, 50°, 70°$; (b) $\phi_T = 45°$, $\phi_R = 20°, 40°, 45°, 50°, 70°$.

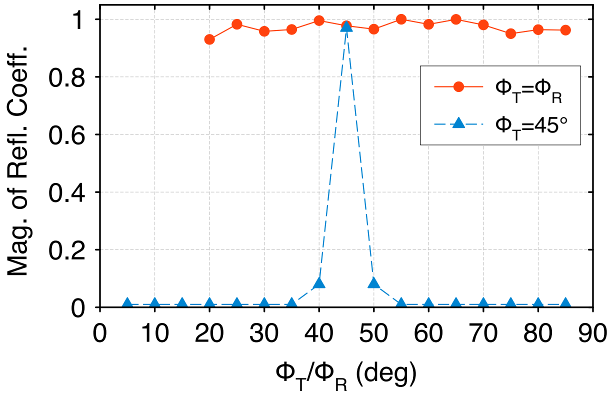

Fig. 18. Measured magnitude of the reflection coefficient of the aluminum reflector used in the R2R RNLoS link: 1) $\phi_T = \phi_R$ in a range from 20° to 85° (red circles); 2) ϕ_T is fixed at 45° while ϕ_R varies from 5° to 85° (blue triangles).

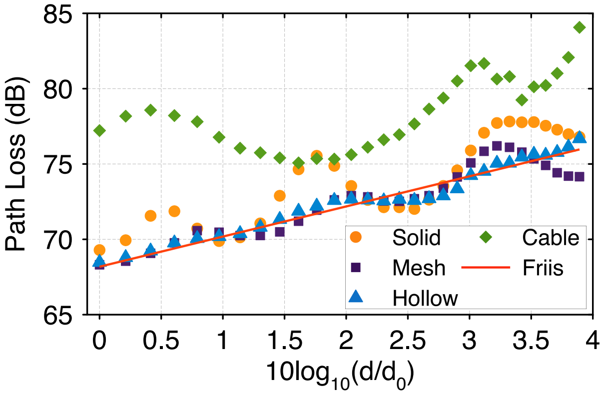

Fig. 19. Friis theoretical path loss (red line) and the measured mean path loss with different vertical ground plane structures: 1) solid metal (yellow circles), 2) hollow structure (blue triangles), 3) mesh structure (purple squares), and 4) hollow structure with cables as obstruction (green diamonds) in the vertical B2B link at d = 20–49 cm and d_0 = 20 cm.

plane structures: 1) solid metal (yellow circles), 2) hollow structure (blue triangles), 3) mesh structure (purple squares), and 4) hollow structure with cables as obstruction (green diamonds) in the vertical B2B link at d = 20–49 cm. It is observed that path loss fluctuates around the theoretical values as distance increases. Specifically, the hollow structure causes the least path loss fluctuation, closely followed by mesh structure, while solid structure creates the most unwanted path loss fluctuation around 4 dB above the Friis path loss. This path loss fluctuation is mainly caused by constructive and destructive interference from two reflected paths: 1) vertical ground plane (path 1 in Fig. 3 (b)) and 2) horizontal ground plane (path 2 in Fig. 3 (b)). Our measurement results show that the vertical ground plane has more dominant effects on the path loss fluctuation than the horizontal ground plane in vertical B2B links since strong path loss fluctuation is observed when solid vertical ground plane is applied (yellow circles in Fig. 19), while without solid vertical ground plane, only slight path loss fluctuation is observed (blue triangles in Fig. 19). As a result, for future THz B2B communication system design, we recommend to use hollow structure instead of solid metal for vertical ground planes on server racks to minimize path loss fluctuation. The following comparisons of measured path loss, PDPs, and B_c for the B2B RNLoS and B2B ORNLoS links are based on the hollow structure design in Fig. 5 (b) since it has the least path loss interference from vertical ground plane.

Note that besides vertical ground plane design, one of the key challenges in designing vertical B2B links is the positioning of the $\mathrm{T_x}/\mathrm{R_x}$ reflectors. Misaligned reflectors may increase path loss and path loss fluctuation, or even cause complete signal loss. Here we briefly discuss the consequences of misaligned reflectors. We use the same hollow vertical ground plane design in Fig. 5 (b) but intentionally tilt the $\mathrm{R_x}$ reflector around 1° away from the original 45° position. Fig. 20 shows the Friis theoretical path loss (red line) and the measured mean path loss with misaligned $\mathrm{R_x}$ reflector (blue triangles) at d = 20–49 cm. It is observed that the misaligned reflector can cause up to 4 dB path loss deviation from the Friis values. Therefore, for future THz B2B link design, we recommend to integrate the $\mathrm{T_x}$/$\mathrm{R_x}$ reflectors into the server racks for better alignment since the received signal is extremely sensitive to the positioning of the reflectors.

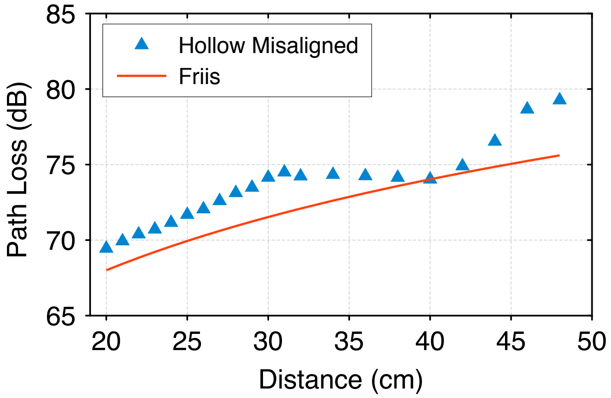

Fig. 20. Friis theoretical path loss (red line) and the measured mean path loss with $\mathrm{R_x}$ reflector tilted (misaligned) by around 1° away from the original 45° position (blue triangles) in the vertical B2B link at d = 20–49 cm.

Next, we compare the measured path loss, PDPs, and B_c between B2B RNLoS and B2B ORNLoS links with hollow vertical ground plane design. Fig. 19 compares the Friis theoretical path loss (red line) and the measured path loss curves in B2B RNLoS (blue triangles) and B2B ORNLoS (green diamonds) scenarios over distances at d = 20–49 cm. Figs. 21 (a) and (b) present the measured path loss curves and Friis theoretical path loss curves over frequencies in B2B RNLoS and B2B ORNLoS scenarios at d = 24, 32, 42 cm. In Fig. 19 (blue triangles) and Fig. 21 (a), the measured path loss curves in the B2B RNLoS link closely follow the Friis values in both distance and frequency domains. In Fig. 19 (green diamonds) and Fig. 21 (b), the measured path loss curves in the B2B ORNLoS link show that cables as obstruction can increase path loss by around 5–10 dB as compared to the B2B RNLoS link and the frequency-dependent path loss fluctuation becomes more prominent at higher frequencies. Note that path loss values in the B2B ORNLoS link in Fig. 19 (green diamonds) and Fig. 21 (b) decrease as distance increases from 24 cm (red circles in Fig. 21 (b)) to 32 cm (blue triangles in Fig. 21 (b)). This is because signals in the direct $\mathrm{T_x}$-$\mathrm{R_x}$ path and reflected path caused by the cables arrive within the same delay bin, i.e., their time difference of arrival (or path length difference) is smaller than the minimum time domain resolution (or spatial resolution) of the measurement system, where signals add up either in-phase or out-of-phase and result in constructive or destructive interference. We have further investigated the shadowing gain (X_σ) in the B2B ORNLoS link by repeating the measurements with three cable thickness sizes and ten cable positions at d = 20–49 cm to have enough ensemble to perform a statistical evaluation. We found that the shadowing gain follows a log-normal distribution with the logarithmic equivalent having a zero-mean (in dB) and standard deviation (σ) of 3.9 dB. A CDF of X_σ for the B2B ORNLoS link is presented in Fig. 13 (c) to confirm the log-normality of the shadowing gain.

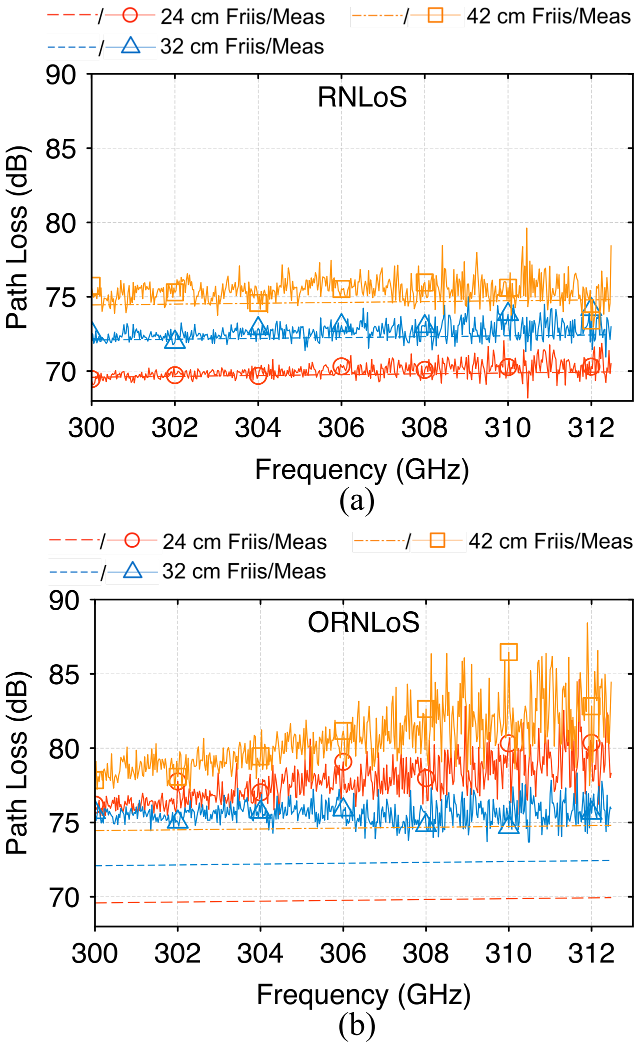

(a)

(b)

Fig. 21. Measured path loss curves and Friis theoretical path loss curves in (a) B2B RNLoS and (b) B2B ORNLoS scenarios at d = 24, 32, 42 cm.

Figures 22 (a) and (b) show the measured PDPs for B2B RNLoS and B2B ORNLoS links at d = 24, 32, 42 cm. In Fig. 22 (a), a dominant multipath cluster at around 1 ns is observed in the B2B RNLoS link, which results from multiple reflection between $\mathrm{T_x}$/$\mathrm{R_x}$ blades since 1 ns corresponds to twice the vertical distance between two blades. In contrast, with cables as obstruction, the multipath cluster at around 1 ns is no longer observable in the B2B ORNLoS link as shown in Fig. 22 (b). In addition, the first arriving peak in Fig. 22 (b) is followed by a "long tail" over 0–0.5 ns, which is a result of multiple reflection between cables that arrives in several adjacent delay bins. A "long tail" in PDPs will generally act as interference and weaken communication performance [40].

Figure 23 shows the measured B_c for B2B RNLoS and B2B ORNLoS scenarios at d = 20–49 cm. It is observed that as distance increases from 20 cm to 49 cm, B_c drops from around 1 GHz to around 0.4 GHz in the RNLoS link while stays relatively constant at around 0.2–0.5 GHz in the ORNLoS link. Results imply that the B2B RNLoS link can achieve higher peak data rate as compared to the B2B ORNLoS link while the data rate in the B2B RNLoS link may fluctuate more as distance varies.

This article has been accepted for publication in a future issue of this journal, but has not been fully edited. Content may change prior to final publication. Citation information: DOI 10.1109/TAP.2019.2949135, IEEE Transactions on Antennas and Propagation

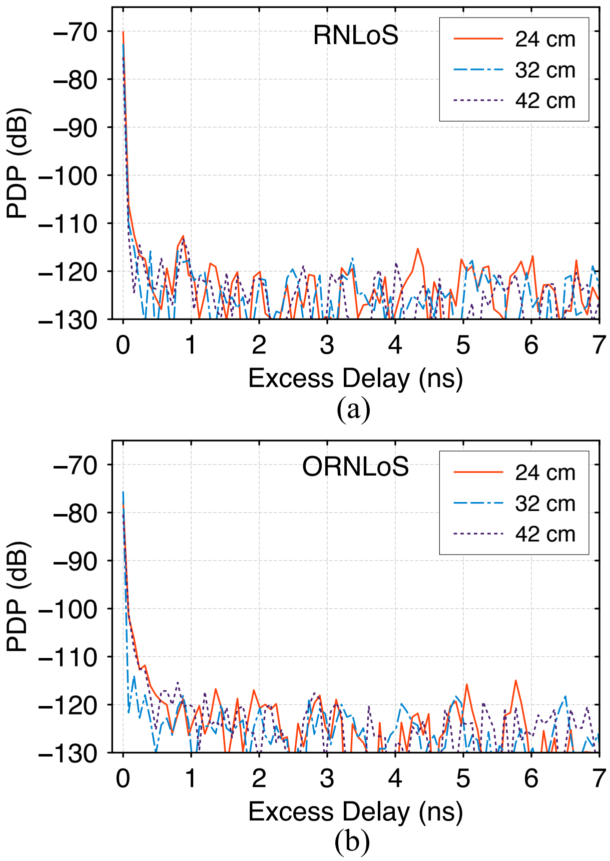

Fig. 22. Measured PDPs for (a) B2B RNLoS and (b) B2B ORNLoS scenarios at d = 24, 32, 42 cm.

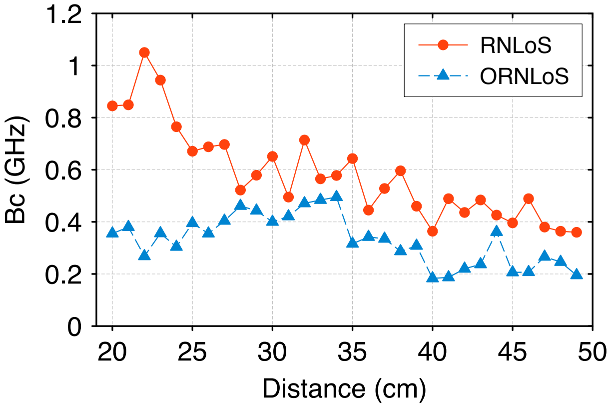

Fig. 23. Measured B_c for B2B RNLoS and B2B ORNLoS scenarios at d = 20–49 cm.

B. Characterization of B2B LoS Link

In this section, we study the relationship between T_x-R_x distance and the corresponding path loss and PDPs in the B2B LoS scenario as introduced in Fig. 4 (e) and Section III-G.

Measured path loss curves and Friis theoretical path loss values for the B2B LoS link are presented in Fig. 24 (a). It can be observed that the measured path loss values closely follow the theoretical values across all distances. The corresponding measured PDPs are presented in Fig. 24 (b). Although being surrounded by metal plates, there is no observable multipath cluster in the PDPs of the B2B LoS link due to very focused beamwidth at THz frequencies. In summary, the B2B LoS link is comparable to the LoS propagation in a free space. Similar measurement results can be found in [34].

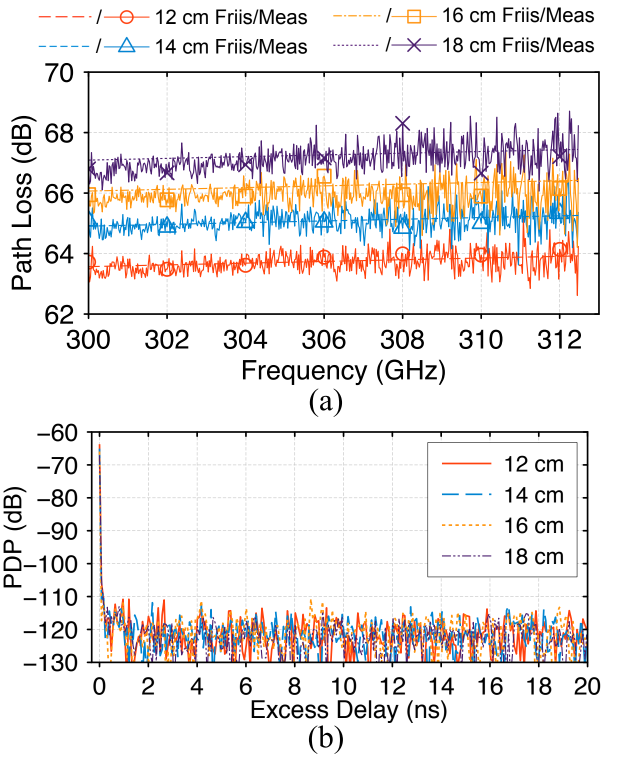

Fig. 24. (a) Measured path loss curves and Friis theoretical path loss values and (b) measured PDPs for the B2B LoS scenario at d = 12, 14, 16, 18 cm.

VII. CONCLUSIONS

This paper presents characterization of 300 GHz channels for wireless R2R and B2B communications in data centers. Measurements are conducted in R2R LoS, R2R OLoS, R2R RNLoS, R2R ORNLoS, B2B RNLoS, B2B ORNLoS, and B2B LoS scenarios, which evaluate the impact of T_x/R_x misalignment and obstructions such as cables, metal cabinets, and mesh structures on THz propagation, as well as possibility of using existing metal objects as reflectors that guide waves for NLoS type of links. For the R2R LoS scenario, the channel with optical lenses acts as a waveguide with a PLE of 1.48 and the optical lenses provide additional gain of more than 25 dB. Multiple reflections are observed in PDPs when lenses are used to extend the distance. When obstructions of cables are present, ORNLoS link performs better than OLoS link with 2.5 dB lower shadowing gain and weaker multipath. Multi-band spectrum utilization [18] may be required in the OLoS link since the lowest B_c is only around 0.3 GHz. Reflector in the RNLoS link has reflection coefficients very close to 1 for all incident angles. For the B2B scenario, a dual-reflector THz transceiver rack system has been proposed to enable wireless links across vertically stacked servers and allow easy maintenance and repair of servers. The measured path loss approximates the Friis values in the LoS link and in the RNLoS link with hollow vertical ground plane. Hollow rack structure is preferred over solid metal due to its minimum reflection interference. When obstructions of cables are present, the ORNLoS link experiences 5–10 dB higher path loss and on average 0.25 GHz lower B_c than the RNLoS link. Measured statistical channel properties show that the shadowing gain caused by cable clusters follows the log-normal distribution.

This article has been accepted for publication in a future issue of this journal, but has not been fully edited. Content may change prior to final publication. Citation information: DOI 10.1109/TAP.2019.2949135, IEEE Transactions on Antennas and Propagation

REFERENCES

[1] Y. Cui, H. Wang, X. Cheng, and B. Chen, “Wireless Data Center Networking,” *IEEE Wireless Communications*, vol. 18, no. 6, pp. 46–53, Dec. 2011.

[2] C. Zhang, F. Wu, X. Gao, and G. Chen, “Free Talk in the Air: A Hierarchical Topology for 60 GHz Wireless Data Center Networks,” *IEEE/ACM Transactions on Networking*, vol. 25, no. 6, pp. 3723–3737, Dec. 2017.

[3] K. Ramachandran, R. Kokku, R. Mahindra, and S. Rangarajan, “60 GHz Data-Center Networking: Wireless = Worry Less?” in *NEC Technical Report*, Jul. 2008.

[4] G. Chen, H. Chen, M. Haurylau, N. A. Nelson, D. H. Albonesi, P. M. Fauchet, and E. G. Friedman, “On-Chip Copper-Based vs. Optical Interconnects: Delay Uncertainty, Latency, Power, and Bandwidth Density Comparative Predictions,” in *International Interconnect Technology Conference*, Jun. 2006, pp. 39–41.

[5] T. Chen, X. Gao, and G. Chen, “The Features, Hardware, and Architectures of Data Center Networks: A Survey,” *Journal of Parallel and Distributed Computing*, vol. 96, pp. 45–74, Oct. 2016.

[6] W. Zhang, X. Zhou, L. Yang, Z. Zhang, B. Y. Zhao, and H. Zheng, “3D Beamforming for Wireless Data Centers,” in *Proceedings of the 10th ACM Workshop on Hot Topics in Networks*, ser. HotNets-X. New York, NY, USA: ACM, Nov. 2011, pp. 4:1–4:6.

[7] X. Zhou, Z. Zhang, Y. Zhu, Y. Li, S. Kumar, A. Vahdat, B. Y. Zhao, and H. Zheng, “Mirror Mirror on the Ceiling: Flexible Wireless Links for Data Centers,” in *Proceedings of the ACM SIGCOMM Conference on Applications, Technologies, Architectures, and Protocols for Computer Communication*, ser. SIGCOMM ’12. New York, NY, USA: ACM, Aug. 2012, pp. 443–454.

[8] D. Halperin, S. Kandula, J. Padhye, P. Bahl, and D. Wetherall, “Augmenting Data Center Networks with Multi-Gigabit Wireless Links,” *SIGCOMM Comput. Commun. Rev.*, vol. 41, no. 4, pp. 38–49, Aug. 2011.

[9] J. Y. Shin, E. G. Sirer, H. Weatherspoon, and D. Kirovski, “On the Feasibility of Completely Wireless Datacenters,” in *ACM/IEEE Symposium on Architectures for Networking and Communications Systems (ANCS)*, Oct. 2012, pp. 3–14.

[10] A. Davy, L. Pessoa, C. Renaud, E. Wasige, M. Naftaly, T. Kürner, G. George, O. Cojocari, N. O. Mahony, and M. A. G. Porcel, “Building An End User Focused THz Based Ultra High Bandwidth Wireless Access Network: the TERAPOD Approach,” in *9th International Congress on Ultra Modern Telecommunications and Control Systems and Workshops (ICUMT)*, Nov. 2017, pp. 454–459.

[11] B. Peng and T. Kürner, “A Stochastic Channel Model for Future Wireless THz Data Centers,” in *International Symposium on Wireless Communication Systems (ISWCS)*, Aug. 2015, pp. 741–745.

[12] L. Popa, S. Ratnasamy, G. Iannaccone, A. Krishnamurthy, and I. Stoica, “A Cost Comparison of Datacenter Network Architectures,” in *Proceedings of the 6th International Conference*, ser. Co-NEXT ’10. New York, NY, USA: ACM, 2010, pp. 16:1–16:12.

[13] L. A. Barroso, J. Clidaras, and U. Höelzle, *The Datacenter as a Computer: An Introduction to the Design of Warehouse-Scale Machines, Second Edition*, 2nd ed. Morgan and Claypool Publishers, 2013.

[14] *Cisco Unified Computing System Site Planning Guide: Data Center Power and Cooling*, Cisco Systems, Inc., San Jose, CA, USA, 2017. [Online]. Available: https://www.cisco.com/c/en/us/solutions/collateral/data-center-virtualization/unified-computing/white_paper_c11-680202.pdf

[15] H. Vardhan, N. Thomas, S. R. Ryu, B. Banerjee, and R. Prakash, “Wireless Data Center with Millimeter Wave Network,” in *IEEE Global Telecommunications Conference GLOBECOM 2010*, Dec. 2010, pp. 1–6.

[16] E. Baccour, S. Foufou, R. Hamila, and M. Hamdi, “A Survey of Wireless Data Center Networks,” in *49th Annual Conference on Information Sciences and Systems (CISS)*, Mar. 2015, pp. 1–6.

[17] S. Kim and A. Zajić, “Characterization of 300-GHz Wireless Channel on A Computer Motherboard,” *IEEE Transactions on Antennas and Propagation*, vol. 64, no. 12, pp. 5411–5423, Dec. 2016.

[18] “IEEE Standard for High Data Rate Wireless Multi-Media Networks–Amendment 2: 100 Gb/s Wireless Switched Point-to-Point Physical Layer,” *IEEE Std 802.15.3d-2017 (Amendment to IEEE Std 802.15.3-2016 as amended by IEEE Std 802.15.3e-2017)*, pp. 1–55, Oct. 2017.

[19] I. F. Akyildiz, C. Han, and S. Nie, “Combating the Distance Problem in the Millimeter Wave and Terahertz Frequency Bands,” *IEEE Communications Magazine*, vol. 56, no. 6, pp. 102–108, Jun. 2018.

[20] N. Khalid and O. B. Akan, “Experimental Throughput Analysis of Low-THz MIMO Communication Channel in 5G Wireless Networks,” *IEEE Wireless Communications Letters*, vol. 5, no. 6, pp. 616–619, Dec. 2016.

[21] J. M. Jornet and I. F. Akyildiz, “Channel Modeling and Capacity Analysis for Electromagnetic Wireless Nanonetworks in the Terahertz Band,” *IEEE Transactions on Wireless Communications*, vol. 10, no. 10, pp. 3211–3221, Oct. 2011.

[22] S. Mollahasani and E. Onur, “Evaluation of Terahertz Channel in Data Centers,” in *NOMS 2016 - 2016 IEEE/IFIP Network Operations and Management Symposium*, Apr. 2016, pp. 727–730.

[23] H. Elayan, O. Amin, R. M. Shubair, and M. Alouini, “Terahertz Communication: the Opportunities of Wireless Technology Beyond 5G,” in *2018 International Conference on Advanced Communication Technologies and Networking (CommNet)*, Apr. 2018, pp. 1–5.

[24] B. Peng, S. Rey, D. M. Rose, S. Hahn, and T. Kürner, “Statistical Characteristics Study of Human Blockage Effect in Future Indoor Millimeter and Sub-Millimeter Wave Wireless Communications,” in *IEEE 87th Vehicular Technology Conference (VTC Spring)*, Jun. 2018, pp. 1–5.

[25] V. Petrov, D. Moltchanov, Y. Koucheryavy, and J. M. Jornet, “The Effect of Small-Scale Mobility on Terahertz Band Communications,” in *Proceedings of the 5th ACM International Conference on Nanoscale Computing and Communication*, ser. NANOCOM ’18. New York, NY, USA: ACM, Sep. 2018, pp. 40:1–40:2.

[26] M. Curran, K. Zheng, H. Gupta, and J. Longtin, “Handling Rack Vibrations in FSO-Based Data Center Architectures,” in *2018 International Conference on Optical Network Design and Modeling (ONDM)*, May 2018, pp. 47–52.

[27] R. Piesiewicz, C. Jansen, D. Mittleman, T. Kleine-Ostmann, M. Koch, and T. Kürner, “Scattering Analysis for the Modeling of THz Communication Systems,” *IEEE Transactions on Antennas and Propagation*, vol. 55, no. 11, pp. 3002–3009, Nov. 2007.

[28] C. Jansen, S. Priebe, C. Moller, M. Jacob, H. Dierke, M. Koch, and T. Kürner, “Diffuse Scattering From Rough Surfaces in THz Communication Channels,” *IEEE Transactions on Terahertz Science and Technology*, vol. 1, no. 2, pp. 462–472, Nov. 2011.

[29] V. Petrov, J. Kokkoniemi, D. Moltchanov, J. J. Lehtomäki, Y. Koucheryavy, and M. J. Juntti, “Last Meter Indoor Terahertz Wireless Access: Performance Insights and Implementation Roadmap,” *IEEE Communications Magazine*, vol. 56, no. 6, pp. 158–165, Jun. 2018.

[30] *Custom Transmitters*, Virginia Diodes, Inc., Charlottesville, VA, USA. [Online]. Available: http://vadiodes.com/en/products/custom-transmitters

[31] *Plano-Convex PTFE Lens*, Thorlabs, Inc., Newton, NJ, USA. [Online]. Available: https://www.thorlabs.com/thorproduct.cfm?partnumber=LAT075

[32] D. Headland, Y. Monnai, D. Abbott, C. Fumeaux, and W. Withayachumnankul, “Tutorial: Terahertz Beamforming, from Concepts to Realizations,” *APL Photonics*, vol. 3, no. 5, pp. 051 101–1–051 101–32, 2018.

[33] *1U, 2U, 3U, 4U, 5U, 6U, and 7U*, Nov. 2018. [Online]. Available: https://www.computerhope.com/jargon/num/1u.htm

[34] C.-L. Cheng, S. Kim, and A. Zajić, “Comparison of Path Loss Models for Indoor 30 GHz, 140 GHz, and 300 GHz Channels,” in *11th European Conference on Antennas and Propagation (EUCAP)*, Mar. 2017, pp. 716–720.

[35] A. Zajić, *Mobile-to-Mobile Wireless Channels*. Norwood, MA, USA: Artech House, Inc., 2013.

[36] T. Rappaport, *Wireless Communications: Principles and Practice*, 2nd ed. Upper Saddle River, NJ, USA: Prentice Hall PTR, 2001.

[37] S. Bhardwaj, N. K. Nahar, and J. L. Volakis, “All Electronic Propagation Loss Measurement and Link Budget Analysis for 350 GHz Communication Link,” *Microwave and Optical Technology Letters*, vol. 59, no. 2, pp. 415–423, Feb. 2017.

[38] M. O. Al-Nuaimi and A. G. Siamarou, “Coherence bandwidth Characterisation and Estimation for Indoor Rician Multipath Wireless Channels Using Measurements at 62.4GHz,” *IEE Proceedings - Microwaves, Antennas and Propagation*, vol. 149, no. 3, pp. 181–187, Jun. 2002.

[39] R. Wang, B. Deng, Y. Qin, H. Wang, and X. Li, “Study of Scattering Characteristics for Metallic Spheres at Terahertz Frequencies,” *Journal of Electromagnetic Waves and Applications*, vol. 28, no. 14, pp. 1786–1797, Jul. 2014.

[40] T. Jenserud and S. Ivansson, “Measurements and Modeling of Effects of Out-of-Plane Reverberation on the Power Delay Profile for Underwater Acoustic Channels,” *IEEE Journal of Oceanic Engineering*, vol. 40, no. 4, pp. 807–821, Oct. 2015.

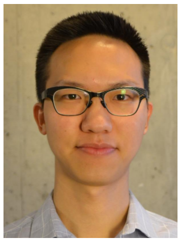

Chia-Lin Cheng (S'17) received the B.Sc. degree in electrical engineering from the National Taiwan University in 2013 and the M.Sc. degree in electrical engineering from the Georgia Institute of Technology in 2017, respectively. He is currently pursuing his PhD in the Electromagnetic Measurements in Communications and Computing (EMC^2) Lab at the Georgia Institute of Technology focusing on mm-wave and THz wireless channel measurements and modeling. Previously, he worked on signal integrity and non-linear circuits I/O modeling by using machine learning techniques. His research interests span areas of electromagnetics, wireless channel measurements and modeling. He was the recipient of the Best Poster Award at the IEEE International Conference on RFID 2018.

Alenka Zajić (S99-M09-SM13) received the B.Sc. and M.Sc. degrees form the School of Electrical Engineering, University of Belgrade, in 2001 and 2003, respectively. She received her Ph.D. degree in Electrical and Computer Engineering from the Georgia Institute of Technology in 2008. Currently, she is an Associate Professor in the School of Electrical and Computer Engineering at Georgia Institute of Technology. Prior to that, she was a visiting faculty member in the School of Computer Science at Georgia Institute of Technology, a post-doctoral fellow in the Naval Research Laboratory, and a design engineer at Skyworks Solutions Inc. Her research interests span areas of electromagnetic, wireless communications, signal processing, and computer engineering. Dr. Zajic was the recipient of the 2017 NSF CAREER award, the Best Paper Award at MICRO 2016, 2012 Neal Shepherd Memorial Best Propagation Paper Award, the Best Student Paper Award at the IEEE International Conference on Communications and Electronics 2014, the Best Paper Award at the International Conference on Telecommunications 2008, the Best Student Paper Award at the 2007 Wireless Communications and Networking Conference, and the Dan Noble Fellowship in 2004, which was awarded by Motorola Inc. and the IEEE Vehicular Technology Society for quality impact in the area of vehicular technology.